Geophysical Research Letters

Supporting Information for

The 15 January 2022 Hunga Tonga eruption history as inferred from ionospheric observations

E. Astafyeva[1], B. Maletckii[1], T. D. Mikesell[2], E. Munaibari[3], M. Ravanelli[1], P. Coisson[1], F. Manta[3], L. Rolland[3]

1 – Université Paris Cité, Institut de Physique du Globe de Paris (IPGP), CNRS UMR 7154, 35-39 Rue Hélène Brion, 75013 Paris, France, email : astafyeva@ipgp.fr
2 – Norwegian Geotechnical Institute, Natural Hazards, Oslo, Norway
3 – Université Côte d'Azur, Observatoire de la Côte d'Azur, CNRS, IRD, Géoazur, 250 rue Albert Einstein, Sophia Antipolis 06560 Valbonne, France.

Contents of this file

Introduction

The supplementary material consists of Texts S1-S2, Figures S1 – S4 and Tables S1 – S5.

Figure S1 illustrates the method of ionospheric localization of the volcanic source.

Figure S2 shows the travel-time diagrams (hodocrones) for TEC data series measured by four satellites: G24 (a), G23 (b), G18 (c) and R20 (d). One can be clearly see the occurrence

of at least 2 main disturbances at ~4.45-4.9 UT and ~5.2–5.7 UT in data of G18 and R20. From the hodocrones, we estimate the apparent velocities to be in the range 555-680 m/s for G23 and G24, 740 m/s for G18 and about 1100 m/s for R20 for both disturbances. We note that this range of velocities correspond to the acoustic waves, which is an additional proof of the observed TEC peaks being driven by explosions.

Figure S3 demonstrates that on the day of the eruption (15 January 2022), the thermospheric composition was decreased over the area of the volcano, as a result of the geomagnetic storm that commenced the day before.

Figure S4 shows TEC variations that capture the response to the explosion at ~08:25UT. This TEC response is very moderate because of the poor ionization due to the large-scale depletion.

Tables S1-S5 present the parameters of CVID used for ionospheric estimation of the onset time for the explosions 1 to 5, respectively, as mentioned in the main text and in Figure 2(b).

All GNSS data are freely available from the CDDIS data archives (https:// https://cddis.nasa.gov/). Data of station RAUL are from the Geological hazard information for New Zealand (GeoNet) FTP-database via ftp://ftp.geonet.org.nz/gps/rinex/. The data of the thermospheric O/N2 composition are available from: http://guvitimed.jhuapl.edu/. The GUVI instrument was designed and built by The Aerospace Corporation and The Johns Hopkins University. The Principal Investigator is Dr. Andrew B. Christensen and the Chief Scientist and co-PI is Dr. Larry J. Paxton.

Text S1

We use an approximation of spherical wave propagating from a point source (*Xs, Ys, Zs*), at constant speed *V* (Kiryushkin & Afraimovich, 2007; Shults et al., 2016). Co-volcanic ionospheric disturbances (CVID) arrive at points (*Xi, Yi, Zi*) at moments of time t_i (Figure S1). The altitude of CVID detection is *Hion* = 320 km, and the source coordinates are taken at the position of the HTHH volcano. First, we find the "reference" point (X_0, Y_0, Z_0) that corresponds to the earliest arrival. Then, we solve a system of equations for the spherical wave travelling from the point source to the reference point (distance $\rho 0$) and to the i_{th} point (distance ρi), and we compute the time delay of the perturbation arrival in registration points. The distance between the reference point and the i_{th} point is

determined as *dρi = ρi-ρ0* (Figure S1). These calculations are made for all possible values in the range of velocity *V* between 600 m/s and 1100 m/s, which is in the range of the acoustic wave speed.

For each combination of parameters, we compute an error between the spherical wave model and the real observations, and the result with the minimal value of the error corresponds to the final solution.

The onset time is calculated from the computed parameters: the propagation velocity *V*, the coordinates of the source (*Xs, Ys, Zs*), and the arrival time *t0* of the disturbance in the reference point:

$$t_s = t_0 - \frac{\sqrt{(x_0 - x_s)^2 + (y_0 - y_s)^2 + (z_0 - z_s)^2}}{V} \quad \text{(S1)}$$

This method was applied to analyze the scenario of the HTHH eruption of 15 January 2022. We first identified peaks with clear N-wave-like signatures that could correspond to an explosion. We note that not every peak in the TEC data series in Figure 2a corresponds to a separate explosion. Some peaks can be artificially formed by the geometry on the GNSS-sounding (as further seen in the simulation results in Figure 3), or some small peaks can represent the gravity waves generated due to the continuous eruption. For such cases, the approximation of spherical wave will not work.

For each selected sub-event, we estimated the arrival time of the CVID and the coordinates of the CVID detection. Further, we launch our algorithm and we find that the peak between events #3 and #4, and the peak after even #5 do not give any realistic solutions, therefore, we consider that they might not correspond to acoustic waves driven by explosions. Other peaks (noted as 1,2,3,4,5 in Figure 2) provided the onset times and the radial velocity values in the range of acoustic waves (Table 1).

Text S2

We model individual explosive events using the IonoSeis package (Rolland et al., 2013, Mikesell et al., 2019). The ratio of specific heat used to derive the sound speed 1D profile is computed from the composition of the atmosphere provided by NRLMSIS 2.0 model (Emmert et al., 2020) at the time and date of the event. The acoustic shock-wave (bipolar pulse) was taken as the first derivative of a Gaussian pulse (i.e., an N-wave):

$$v(\vec{r},t) = A_z(\vec{r})\frac{A_0\sqrt{2}}{\sigma^{3/2}\pi^{1/4}}(t-t_0)\,e^{-\frac{(t-t_0)^2}{\sigma^2}} \quad \text{(S2)}$$

where t_0 is the time of maximum particle motion; σ is the pulse width in seconds; A_0 is the initial amplitude factor, which scales the amount of energy injected in the atmosphere from the point source (Dautermann et al., 2009; Mikesell et al., 2019); and *Az* is an amplitude factor that describes how the phase and amplitude are affected by frequency-dependent viscous and thermal losses with altitude. The broadening of the pulse due to dispersion upon its propagation is taken into account as:

$$\sigma(\vec{r},t) = bt_w \quad \text{(S3)}$$

where *b* is a scale factor so that the pulse width increases with propagation time. Here *b* was set to 0.04 except the third event that has a *b* factor of 0.01.

The initial atmosphere model is in steady state for each individual simulation. Therefore, we know that at later times after the ionosphere has been disturbed, for instance after the large shock wave, that our initial model is likely incorrect. Therefore, in this study we do not put emphasis on matching the shape of N-waves at later times. This will be the study of future work on the IonoSeis package. However, at early time when our initial model is more valid we do expect to be able to match not just arrival times, but also the waveform shape by adjusting the amplitude (A_0) and the broadening factor *b* (see Mikesell et al. (2019) for more information on modeling parameters).

Figures

Figure S1: (a) Approximation of a spherical wave propagating at a constant speed from a point source with coordinates (*Xs, Ys, Zs*). The eruption onset time is *Ts*. The CVID are detected at points (*Xi, Yi, Zi*) at time moments t_i. The altitude of CVID detection is *Hion* = 320 km; **(b)** Detection points are defined at the moment of time when the TEC starts to significantly increase. For these points, we find the coordinates at the altitude of 320 km. These parameters are further used for the spherical wave algorithm to determine the onsets of the sub-events. Smaller peaks between events 3 and 4, and the peak after event 5 did not give solutions within the spherical wave approximation.

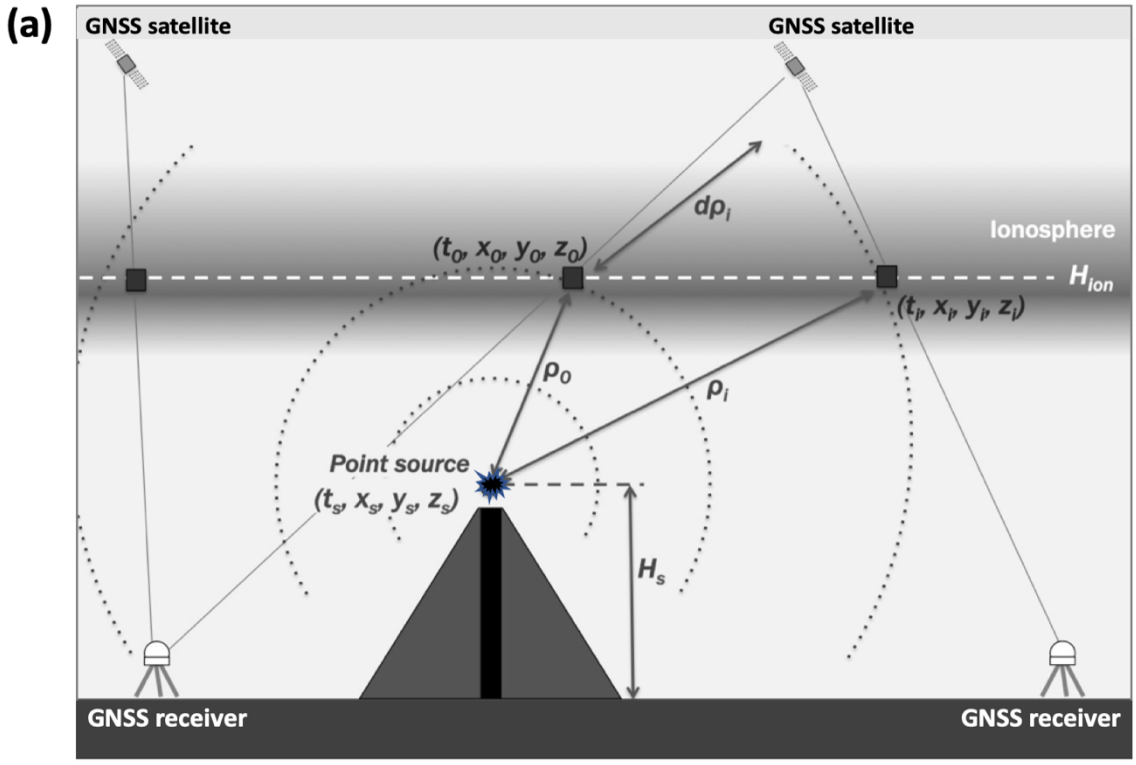
(a)
GNSS satellite
GNSS satellite
Ionosphere
H_{ion}
(t_0, x_0, y_0, z_0)
$d\rho_i$
(t_i, x_i, y_i, z_i)
ρ_0
ρ_i
Point source
(t_s, x_s, y_s, z_s)
H_s
GNSS receiver
GNSS receiver

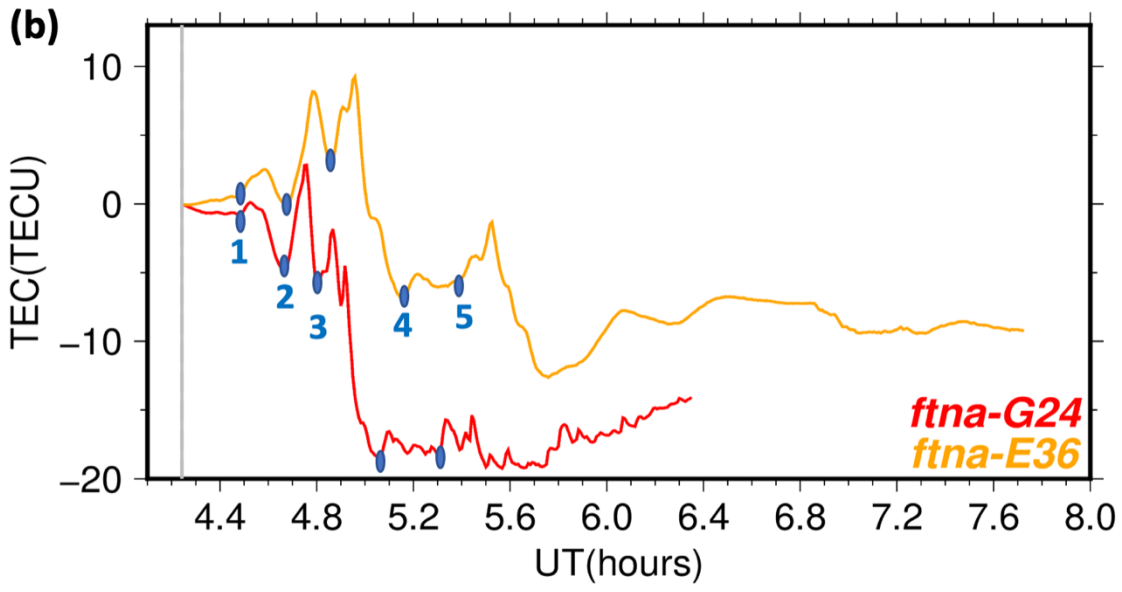
(b)
TEC(TECU)
10
0
−10
−20
1
2
3
4
5
ftna-G24
ftna-E36
4.4
4.8
5.2
5.6
6.0
6.4
6.8
7.2
7.6
8.0
UT(hours)

Figure S2: Travel-time diagrams (hodocrones) for relative unfiltered VTEC for satellites G24 **(a)**, G23 **(b)**, G18 **(c)** and R20 **(d)**. The apparent velocities are 680 m/s (a), 555 m/s (b), 740 m/s (c) and 1100 m/s (d).

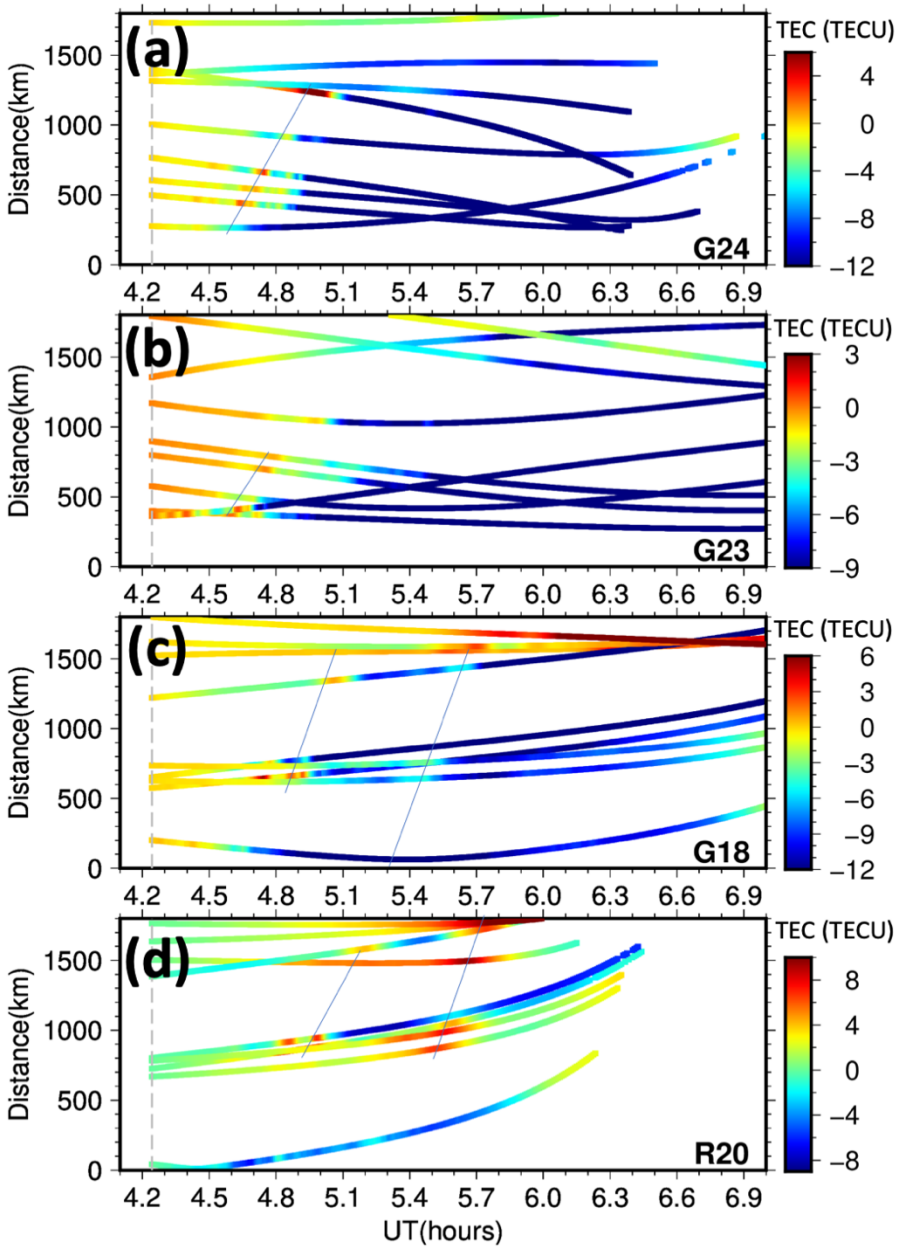

Figure S3: Thermospheric O/N2 composition changes on 13-16 January 2015. The GUVI instrument measures a narrow swath below the satellite at 625 km altitude during the dayside spacecraft passages [Christensen et al, 2003]. The figures show O/N2 data smoothed over 14.9 daily orbits. Red circle in lower left indicates the volcano position (175.382W; 20.536S). We suspect that the composition changes reinforced the ionospheric TEC depletion that was produced by the eruption-driven shock wave. It is known that the composition has a drastic impact on the ionization (Prölss, 1976; Fuller-Rowell et al., 1994). An increase in the molecular species causes an increase in the ionization loss rate, and a decrease of atomic oxygen causes a decrease of the ionization production rate; both these phenomena lead to the ionization decrease.

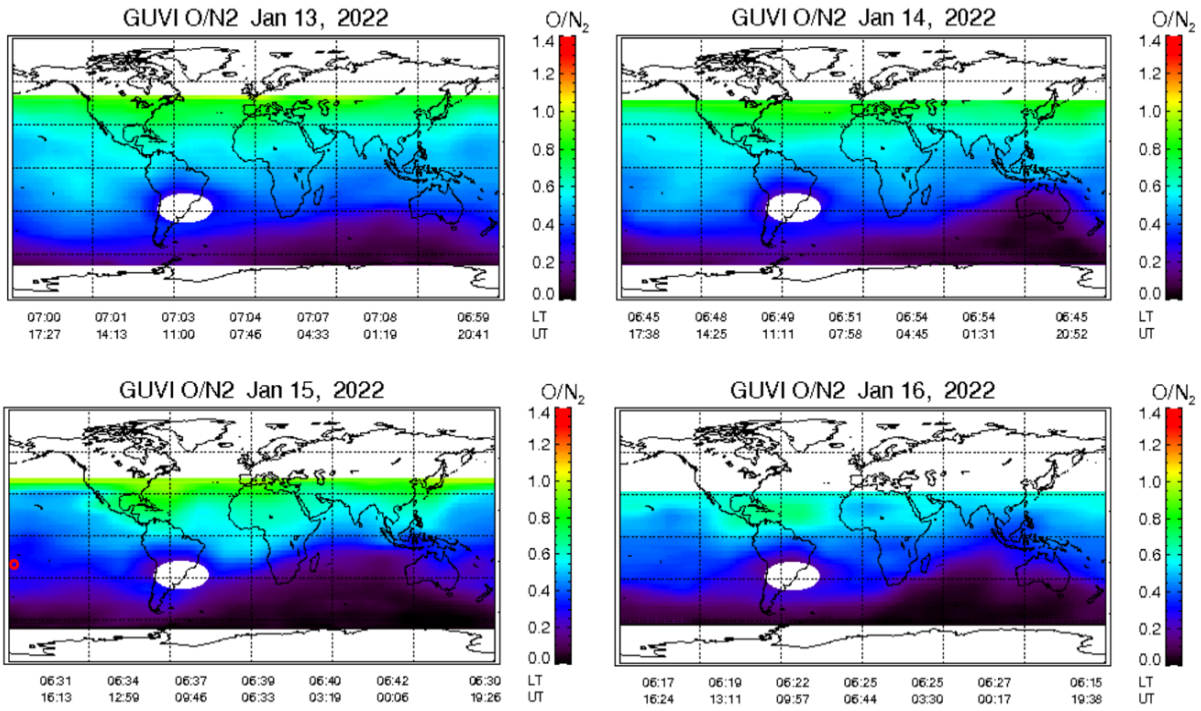

Figure S4: Ionospheric TEC series showing the response to the event that apparently took place ~8:25UT. Arrows show the CVID. We could not analyze this event in detail at this time.

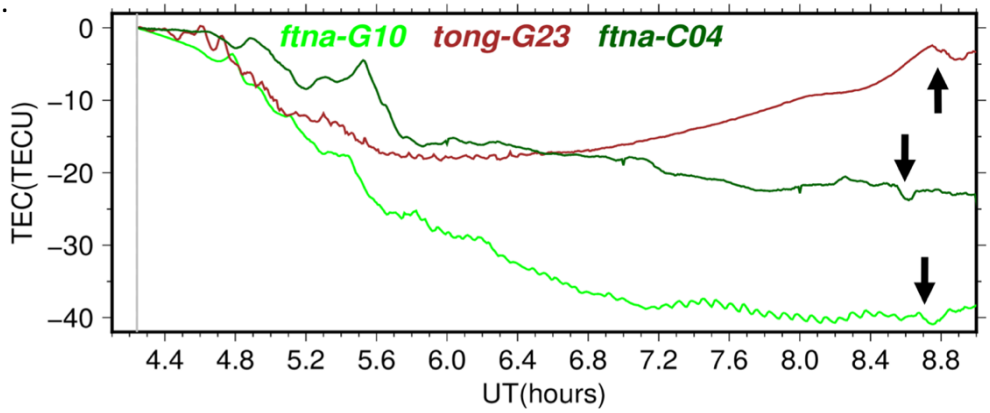

Tables

Table S1: Parameters of the first explosion (marked as #1 in Figure 2b) and the first CVID arrivals (LOS, arrival time Tarr in 30-sec epochs and the coordinates) that were used for estimation of the time onset of this explosion.

LOS	Tarr (30-sec epoch)	CVID arrival (Lon; Lat)
tong G18	527	184.807899; -22.129765
ftna G18	533	182.068450; -15.712337
samo G18	536	188.093275; -15.246549
tong G24	520	187.182446; -20.184082
usp1 G24	523	181.408881; -17.465429
laut G24	525	180.509488; -17.001210
ftna G24	531	184.382928; -14.003524
samo G24	554	190.173092; -13.874976
tuva G24	569	181.980145; -9.247600
tong E36	525	185.187366; -21.147390
usp1 E36	535	179.212216; -18.247160
ftna E36	537	182.422515; -14.607802
samo E36	540	188.419278; -14.132946

Table S2: Parameters of the arrivals of the explosion #2 (LOS, arrival time Tarr in 30-sec epochs and the coordinates) that were used for estimation of the time onset of this explosion.

LOS	Tarr (30-sec epoch)	CVID arrival (Lon; Lat)
tong E36	536	185.196055 -21.030285
usp1 E36	560	179.233677 -17.973405
ftna E36	561	182.433704 -14.346967
samo E36	570	188.422216 -13.809916
tong G18	554	184.934439 -21.797559
ftna G18	558	182.183594 -15.379847
samo G18	561	188.198567 -14.906396
tong G24	531	187.165347 -20.359883
usp1 G24	554	181.365958 -17.979022
laut G24	555	180.469822 -17.503483
ftna G24	560	184.384855 -14.451798
samo G24	574	190.191415 -14.159892
tuva G24	588	182.027249 -9.569821

Table S3: Parameters of the arrival of the disturbance #3 (LOS, arrival time Tarr and the coordinates) that were used for estimation of the time onset of this explosion.

LOS	Tarr (30-sec epoch)	CVID arrival (Lon; Lat)
ftna E36	583	182.438294 -14.105951
samo R20	593	187.850709 -12.739478
samo G24	593	190.219516 -14.433240
usp1 R20	586	178.735076 -16.851442
usp1 E36	583	179.247208 -17.715818

Table S4: Parameters of the arrival of the sub-event #4 (LOS, arrival time Tarr and the coordinates) that were used for estimation of the time onset of this explosion.

LOS	Tarr (30-sec epoch)	CVID arrival (Lon; Lat)
ftna G24	608	184.447810 -15.201575
ftna G18	617	182.371307 -14.619722
ftna E36	619	182.438051 -13.701351
samo G24	616	190.270918 -14.772845
samo E36	616	188.409984 -13.315402
samo G18	611	188.342906 -14.256654

Table S5: Parameters of the arrival of the sub-event #5 (LOS, arrival time Tarr in 30-sec epoch time and the coordinates) that were used for estimation of the time onset of this explosion in the approximation of a spherical wave propagation.

LOS	Tarr (30-sec epoch)	CVID arrival (Lon; Lat)
tong G24	617	187.149439 -21.640964
raul G24	660	184.813518 -29.884852
laut G24	631	180.528565 -18.763369
ftna G24	637	184.537825 -15.684248
samo R20	645	187.762099 -11.706563
ftna G18	643	182.429305 -14.286506
ftna E36	646	182.434860 -13.383897
usp1 E36	637	179.266049 -17.073611
usp1 G18	634	179.215389 -18.010305
ftna R20	636	181.866997 -12.334771

References

Christensen, A. B., et al. (2003), Initial observations with the Global Ultraviolet Imager (GUVI) on the NASA TIMED satellite mission, *J. Geophys. Res*., 108(A12), 1451, doi:10.1029/2003JA009918.

Dautermann, T., E. Calais, and G. S. Mattioli (2009), Global Positioning System detection and energy estimation of the ionospheric wave caused by the 13 July 2003 explosion of the Soufrière Hills Volcano, Montserrat, *J. Geophys. Res*., 114, B02202, doi:10.1029/2008JB005722.

Emmert, J. T., Drob, D. P., Picone, J. M., Siskind, D. E., Jones, M. Jr., Mlynczak, M. G., et al. (2020). NRLMSIS 2.0: A whole-atmosphere empirical model of temperature and neutral species densities. *Earth and Space Science*, 7, e2020EA001321. https://doi.org/10.1029/2020EA001321

Fuller-Rowell, T. J., Codrescu, M. V., Moffett, R. J., & Quegan, S. (1994). Response of the thermosphere and ionosphere to geomagnetic storms. *Journal of Geophysical Research*, 99(A3), 3893–3914. https://doi.org/10.1029/93JA02015

Kiryushkin, V.V. and E.L. Afraimovich (2007) Determining the Parameters of Ionospheric Perturbation Caused by Earthquakes Using the Quasi-Optimum Algorithm of Spatiotemporal Processing of TEC Measurements, *Earth Planets Space*, 2007, vol. 59, pp. 267–278.

Mikesell, T.D.; Rolland, L.M.; Lee, R.F.; Zedek, F.; Coïsson, P.; Dessa, J.-X. (2019) *IonoSeis*: A Package to Model Coseismic Ionospheric Disturbances. *Atmosphere*, *10*, 443. https://doi.org/10.3390/atmos10080443

Pröss, G. W. (1976) On explaining the negative phase of ionospheric storms, Planet. Space Sci., 24, 607-609.

Rolland, L. M., M. Vergnolle, J.-M. Nocquet, A. Sladen, J.-X. Dessa, F. Tavakoli, H.R. Nankali, and F. Cappa (2013), Discriminating the tectonic and non-tectonic contributions in the ionospheric signature of the 2011, Mw7.1, dip-slip Van earthquake, Eastern Turkey, *Geophys. Res. Lett.*, 40, doi:10.1002/grl.50544.

Shults, K., E. Astafyeva and S. Adourian (2016). Ionospheric detection and localization of volcano eruptions on the example of the April 2015 Calbuco events. *J. Geophys. Res. - Space Physics*, V.121, N10, 10,303-10,315, doi:10.1002/2016JA023382.